

Published in final edited form as:

Comput Methods Programs Biomed. 2010 January ; 97(1): 62. doi:10.1016/j.cmpb.2009.07.009.

Automation process for morphometric analysis of volumetric CT data from pulmonary vasculature in rats

Rahul Shingrani¹, Gary Krenz^{1,2,3,4}, and Robert Molthen^{1,2,4}

¹Department of Biomedical Engineering, Marquette University, Milwaukee, WI

²Research Service, Zablocki VA Medical Center, Milwaukee, WI

³Mathematics, Statistics, and Computer Science, Marquette University, Milwaukee, WI

⁴Department of Medicine: Pulmonary and Critical Care, Medical College of Wisconsin, Milwaukee, WI

Abstract

With advances in medical imaging scanners, it has become commonplace to generate large multidimensional datasets. These datasets require tools for a rapid, thorough analysis. To address this need, we have developed an automated algorithm for morphometric analysis incorporating A Visualization Workshop computational and image processing libraries for three-dimensional segmentation, vascular tree generation and structural hierarchical ordering with a two-stage numeric optimization procedure for estimating vessel diameters. We combine this new technique with our mathematical models of pulmonary vascular morphology to quantify structural and functional attributes of lung arterial trees. Our physiological studies require repeated measurements of vascular structure to determine differences in vessel biomechanical properties between animal models of pulmonary disease. Automation provides many advantages including significantly improved speed and minimized operator interaction and biasing. The results are validated by comparison with previously published rat pulmonary arterial micro-CT data analysis techniques, in which vessels were manually mapped and measured using intense operator intervention.

Keywords

automated; vessel; measurement; segmentation; morphometry; 3-D; CT

Introduction

There have been several technological developments in medical imaging scanners in recent years, leading to substantially increased capabilities. Such advances continue to benefit medical researchers and doctors, and the patients they serve. There now exist 'sub-second multi-slice' CT scanners and post-acquisition reconstruction schemes capable of generating large three-dimensional (3-D) data sets detailing the anatomy of various organs [1-3]. Researchers also utilize micro-CT scanners to generate a detailed structural and functional understanding of

All authors can be contacted at the following address: (Dr. Molthen is the corresponding author), Research Service 151, Zablocki VA Medical Center, 5000 West National Avenue, Milwaukee, WI 53295, R.S.: (414) 364-3377 / rshingrani@gmail.com, G.K.: (414) 288-6345 / gary.krenz@marquette.edu, R.M.: (414) 384-2000 x41440 or x41439 / rmolthen@mcw.edu.

Publisher's Disclaimer: This is a PDF file of an unedited manuscript that has been accepted for publication. As a service to our customers we are providing this early version of the manuscript. The manuscript will undergo copyediting, typesetting, and review of the resulting proof before it is published in its final citable form. Please note that during the production process errors may be discovered which could affect the content, and all legal disclaimers that apply to the journal pertain.

small animal and biological systems. Current scanners allow high spatial and temporal resolution enabling the study of the etiology and progression of disorders in greater detail than was previously possible. Many of these new imaging methods give rise to very large datasets. For example, in our studies, a single micro-CT volume/image of the rat pulmonary vascular structure is more than 400 MB, resulting in significant challenges in analyzing data efficiently. Applying a manual or semi-automated protocol to detect vessels, map their 3-D coordinates, measure lengths and diameters requires extensive operator interaction. In practice, this limits the measurements to a subset of the entire vascular tree. These impediments provided the motivation to develop an automated technique for faster, more complete morphometric analysis.

One of the primary objectives of our group has been to develop a structural and functional understanding of pulmonary vascular remodeling (PVRem). PVRem is defined by cellular and structural changes in the normal architecture of the walls of pulmonary vessels, which typically lead to an increase in the pulmonary vascular resistance. The increased resistance results in an increase in the intravascular pressure, defined as pulmonary hypertension (PH), which then perpetuates the remodeling. Thus, PVRem involves a vicious cycle, which eventually leads to cor pulmonale and death. In order to design therapies, a fundamental understanding of the development of PVRem is important. To approach this goal, our lab studies the pulmonary arterial structure in the rat using micro-CT images obtained over a range of constant intravascular pressures.

We have previously developed a robust operator guided manual technique for morphometric analysis that combines manual and semi-automated methods [4]. In this previous operator guided manual technique (*OGMT*), an operator laboriously indexed slice-by-slice through the image volume and mapped the 3-D coordinates of the medial axis at anatomical landmarks along the main pulmonary arterial tree. After the coordinates of the main trunk were mapped, a Matlab (MathWorks, Natick, MA) algorithm was used to load the image volume and the coordinates of the medial axis inlet and outlet for each vessel segment. The algorithm then calculated segment length and determined the midpoint of each segment from which to extract a two-dimensional (2-D) slice of data orthogonal to the medial axis. The operator was required to manually adjust the slice data to ensure it contained the appropriate, orthogonal vessel cross-section, mask any adjacent objects that were included in the slice, and then monitor the vessel fitting and diameter estimation procedure to determine the diameter at each segment midpoint. In this study, the process of mapping the vascular tree, slice extraction, background masking and vessel fitting has been completely automated and consequently produces a more comprehensive and efficient morphometric interpretation of the data. Additionally, the proposed algorithm significantly reduces the operator effort and allows measurement of the entire vascular tree while at the same time increasing the consistency of analysis by virtually eliminating operator decision support. Using the algorithm presented in this study, effectively the only operator decision required involves identifying the main arterial trunk, a processed used primarily to compare retrospective data. Although many authors have reported automated segmentation of vasculature [5-11], including work focused on pulmonary vessels[12-17], the work reported here is the first to our knowledge that uses hierarchical vessel ordering and an automated optimized multidimensional, constrained non-linear fitting technique to estimate vessel diameter. Because our segmentation and ordering isolates and maps the entire pulmonary arterial tree, measurement of the complete tree could explicitly and readily be performed. However, the specific algorithm we presented here restricted measurement to the main pulmonary trunk so that the data could be directly applied to our previously developed morphometric models as well as be compared with existing data that was manually measured.

Methods

To develop the automated vessel detection and measurement application (AVDMA), we implemented multiple software tools. C programming language and Tool Command Language (Tcl) and the accompanying graphical user interface Tool Kit (Tk) software were used in combination with A Visualization Workshop (AVW) library of image processing functions. Development was performed under the Linux operating system. Analyze®, a biomedical image analysis software, and the AVW library of functions was licensed through the Biomedical Imaging Resource (BIR) at the Mayo Clinic[18-20]. AVW libraries form the basis of the commercially available software Analyze®, which means that the functionality of Analyze® can be replicated in its entirety and customized programs created using algorithms defined by problem specific applications.

A. Biologic data for design and validation

Data acquired for other ongoing studies was used in the design and validation procedures of the AVDMA. In experiments approved by the local VA Institutional Animal Care and Use Committee (IACUC) and animals treated in accordance with 'The Guide for the care and use of laboratory animals', Sprague-Dawley (SD) rats, weights ranging from 250 - 300 grams, were either exposed to chronic hypoxia (CH, 10% O₂) or normoxia (21% O₂) for 21 days. Their lungs were then excised and the arteries filled with a radio-opaque contrast medium (perfluorooctyl bromide or perflubron) and scanned with the Keck functional imaging center's microfocal X-ray CT system. This is a custom build imaging system composed of a Fein-Focus-100.50 X-ray source (3µm focal spot), a North American Imaging AI-5830-HP image intensifier coupled to a Silicon Mountain Design SMD 1M-15 CCD camera, and a New England Affiliated Technologies specimen micromanipulator stage mounted on a precision rail with position information provided by Mitutoyo linear encoders. The X-ray source voltage was set to 41 kV and current to 140 µA. The lungs were rotated in the X-ray beam at 120°/min and planar images captured at 1° increments to obtain 360 images (512 × 512 pixels) over 3 minutes. For the first scan, a hydrostatic intravascular pressure was set to 30 mmHg (Pa1), and then the pressure was successively lowered to 21, 12 and 5.4 mmHg (Pa2, Pa3, Pa4, respectively) to obtain data at four discrete arterial pressures. The Feldkamp cone-beam reconstruction algorithm [21] was applied to planar images to obtain isotropic reconstructed volumetric datasets, 497 × 497 × 497 voxels in dimension. Further description of the CT system, data acquisition methods, animal models, lung preparation and imaging techniques have been described previously [4,22,23]. Although the algorithm has been developed for our models of pulmonary hypertension in isolated rat lungs, its utility is not limited to non-clinical data sets. The algorithm can be applied to clinical data in which the pulmonary vascular lumen has sufficient contrast from its surrounding. The recursive portion of the algorithm that is used to detect the pulmonary tree at different intravascular pressures would not be directly applicable, since intravascular pressures are never hydrostatic *in vivo*.

B. Algorithm overview

The primary objective of developing the AVDMA was to create an automated application analogous to the OGMT. We accomplished this by modifying and improving the default tree segmentation tool provided in Analyze® to map the medial axis of the pulmonary vasculature and then implemented a unique automated diameter estimation scheme to measure vessel diameters. Figure 1 illustrates the algorithm overview, details of which are subsequently provided.

Reconstructed image data (8-bit unsigned char) acquired at the highest arterial pressure (30 mmHg) was imported into an AVW 'volume structure', a global threshold was used, and a number of image-processing routines were applied to skeletonize the arterial tree. The

skeletonized tree was segmented and the main arterial trunk was isolated using hierarchical mapping in addition to two anatomical locations, the inlet to the main lobar arterial trunk and a distal point along the main trunk, identified by the operator. After the main trunk was isolated it was extended using an adaptive thresholding routine, to include smaller, more distal vessels than the original global threshold provided. The 3-D coordinates of the medial axis identified in the main trunk were used to estimate cumulative trunk length and also to provide the locations at which to extract cross-sectional data on the vessels, used to estimate their diameter. Data extraction and diameter estimation was performed completely autonomously. At each point along the medial axis, the algorithm optimized and extracted an orthogonal slice through the vessel and then implemented a two-stage Modified Gaussian Function (MGF) fitting procedure previously described [4]. The distal coordinates of the main trunk medial axis determined for each current intravascular pressure data set were used as a guide to isolate the main trunk in data from each subsequent (lower) arterial pressure. Identification of the main arterial trunk from each successive pressure data set was performed using a backward mapping technique, taking advantage of the hierarchical ordering provided by the AVW tree analysis functions. By using this hierarchical mapping technique, we ensured that all but a small distal portion of the pathway isolated at each pressure was identical. Length and diameter estimation of the isolated trunk was performed similarly for data from each intravascular pressure. Having diameter measurements of the same vascular pathway over a range of intravascular pressures is important for representative estimates of vessel distensibility.

C. Algorithm details

C1. Generation of skeletonized tree structure—The skeletonized structure generation is a 7-step process, illustrated in Figure 2. The individual steps are explained below:

i. Data Import: Raw isotropic data is read and imported into a standard AVW memory structure.

ii. Thresholding: A binary data structure is a pre-requisite to many segmentation operations, and was generated by thresholding the input volume. Gray scale intensities between user-defined lower and upper threshold values were converted to 1 (foreground) and all other voxels were converted to 0 (background). The conditions for deciding the minimum and maximum threshold values represented a compromise in order to include the maximum possible vascular data and exclude the extrinsic noise. To accomplish this, the upper threshold value was set to the maximum gray scale number (GSN) on an 8-bit grayscale range, i.e., 255, where the higher GSN values represented foreground voxels. The lower threshold value, which was determined by visual inspection method in accordance with the above stated conditions, was set at the GSN value of 60. A histogram for an example CT volume from a control lung is shown in Figure 3. The upper and lower thresholds were used on all lung datasets. Note that this thresholding and binarization was used only to determine the initial medial axis skeleton, the original gray scale data was used to perform adaptive thresholding (with threshold values below 60 to map more distal vessels) and to perform all diameter estimations, see the Adaptive thresholding and Vessel fitting and diameter estimation sections.

iii. Fill Holes: Holes, defined as 0-valued voxels surrounded by neighbors that are 1-valued voxels within the binary volume, needed to be replaced with foreground voxels to proceed with the skeletonization of the vascular network, since the 2-D morphological operations of dilation and erosion that are combined for skeletonization require a 'hole free' volume structure. The AVW_FillHoles function converts isolated, 0-valued voxels to 1-valued pixels, thereby removing the 'holes' in the data.

iv. Thinning (Skeletonization): Based on an algorithm proposed for the skeletonization of 3-D images [9], thinning reduces the vascular network to its respective medial axis, such that each vessel is reduced to a single voxel in diameter. This was accomplished by successive erosion and dilation operations that thin the tree to its skeleton, see Figure 4. Thinning facilitated the subsequent creation of a ‘statistical’ tree that was then used for quantification of the vascular network.

v. Identification of disconnected trees (region-growing): Disconnected or isolated sub-regions can be formed by image artifacts or regions in which the GSN falls outside of the thresholds imposed. It was essential for our algorithm to determine regions that are connected in 3-D space. Reestablishing connectivity was accomplished on the thinned volume using the AVW function ‘AVW_FindVolumeComponents’ that detects 3-D connected regions based on an unseeded (symmetric) region-growing algorithm that sorts individual sub-regions according to size, based on the number of included voxels. 3-D connectivity was determined using a 26-voxel neighborhood. The largest subregion was considered the primary region of interest, since it represented the majority of the vascular tree and our subsequent quantification focused on this sub-region.

vi. Making the tree: The AVW_MakeTree function creates a tree structure from the largest connected component of the thinned vascular network and was utilized to generate the tree structure. The resulting tree structure contains 3-D coordinates of the skeletonized vascular network.

vii. Tree Analysis: Multiple parameters, such as the cross-sectional area of vessel segments, distance between specified points, branching pattern, etc., were calculated using the tree structure and the AVW_TreeAnalysis function. This function defines each node of the tree by an index number, using a letter of the alphabet followed by a number. These indices characterize the branching pattern and create a structured hierarchical nomenclature. At each bifurcation, the index increments to the next letter of the alphabet and number representing the child branch, see Figure 5. This indexed mapping can then be traversed to locate information at locations throughout the vascular network. The AVW_TreeAnalysis routine creates both a detailed and a summarized statistical file of morphological parameters throughout the tree, which were subsequently utilized to identify specific pathways in the tree structure.

C2. Identification of the main arterial trunk—Having generated a map of the vascular structure, the next task was to identify specific pathways in the complex network to study the structural characteristics of the vascular tree. An estimate of vessel distensibility can be made from diameter measurements of identical vessel segments over a range of intravascular pressures. The manual quantification method, developed previously by our group, was designed to incorporate data reduction and was based on the principle that a pulmonary vascular network has a self-consistent structural pattern. Data reduction was achieved by measuring the dimensions of only the vessels that make up the main trunk of the tree and its immediate branches, where the main trunk is the route followed from the inlet pulmonary artery by taking the largest diameter branch at each successive bifurcation. For calibration of the AVDMA algorithm, we chose to identify and measure the main trunk and compare the results with previously measured data on the main trunk. To ensure the main trunk identified with the AVDMA maps the same vessel segments at each of the intravascular pressures, the design of the path-mapping algorithm for the lower three intravascular pressures was altered slightly.

i. Main trunk identification at the highest intravascular pressure: The identification algorithm for the highest intravascular pressure was divided into 2 phases, referred to as the reverse trace (hierarchical mapping) and the forward trace (adaptive thresholding). The

hierarchical structure generated by the 'AVW_TreeAnalysis' function was utilized in the main trunk identification. The reverse trace algorithm segmented a portion of the main trunk, starting from a distal, user-identified, vessel segment and ending at the inlet (the main pulmonary artery), also identified by the user. The forward trace algorithm then identified the remaining main trunk, starting from the distal segment defined by the user and extending to the most distal segment detected (Figure 6). To identify a distal segment at a location along the main trunk, the Tree Analysis module of the Analyze® software package was utilized. The user selects a distal segment of the main trunk that can be easily identified (see location [a] in Figure 6). Analyze® allows determination of the segment name at that location using the 'Tree Map' feature performed by clicking on the 3-D location. The user also identifies the location of the inlet using the Analyze® Tree Analysis module. Using these points, the reverse trace phase of the algorithm then maps the section of the main trunk from the distal, user-selected point, to the inlet.

The forward trace algorithm (Figure 7), maps the remainder of the pathway. The forward trace algorithm was designed to make decisions at each successive bifurcation, based on the characteristics of the pulmonary vasculature. The algorithm compares the measurements of the 2 bifurcating branches taking into consideration cross-sectional vessel diameters, vessel segment length and standard deviation of the vessel segment area. A special factor was also designed to address inconclusive comparisons between the two bifurcating branches. This factor forced a decision based on branch length and the vessel cross-sectional area standard deviation (condition 2 in Figure 7).

ii. Main trunk identification at the lower intravascular pressures: The primary objective for designing an altered algorithm for pathway identification at the lower intravascular pressures was to ensure accurate quantification of structural changes in the selected vessel segments. The pathway mapped at the highest intravascular pressure was used as a 'guide' to map pathways at the remaining pressures. Mapping of the selected pathway at lower pressures was achieved by applying the reverse trace algorithm, initiated near the end-point of the pathway determined by the algorithm at the highest intravascular pressure. Assuming relatively small and uniform spatial translation of the distal tree, the end-point for each successive datasets (lower-pressure) was located by a simple search on each consecutively skeletonized tree for the segmented point closest to the end-point of the preceding (higher-pressure) dataset. With this location as the start point, the reverse trace phase of the algorithm mapped the main trunk back to the inlet. Figure 8 illustrates identical pathways at the lowest and highest intravascular pressures.

C3. Adaptive thresholding—An objective of designing an adaptive thresholding routine was to enable the identification and subsequent quantification of the most distal vessel segments, which were not included within the original threshold limits, and thus, in the initial mapping. This was achieved by applying iterative, regional segmentation to the original gray scale CT data at successively lower thresholds (< 60) to increasingly smaller sub-volumes of data centered on the end-point of the previously mapped segment. The organizational flowchart depicting the adaptive thresholding process is illustrated in Figure 9. Small, distal vessels identified by this routine were appended consecutively to the end of the initially identified pathway.

C4. Diameter Calculation using the Modified Gaussian Function—A combination of the Full Width at Half Maximum (FWHM) and the Brightness Area Product (BAP) techniques was developed by our group to measure vessels ranging from a several millimeters to tens of microns, smaller than the Standard Deviation (SD) of the Point Spread Function (PSF) [4]. The algorithm was designed to estimate vessel diameters using a model of the physical system and blurring introduced by the reconstruction algorithm. Diameters of the

vessel segments identified by the AVDMA were estimated by fitting data from 2-D slices extracted from the original gray scale CT volume. The slices are oriented orthogonal to the vessel central or medial axis using cubic-spline interpolation and then fit to a Modified Gaussian Function (MGF). Figure 10 provides an overview of the diameter estimation algorithm.

The algorithm was designed to first perform a multi-slice calibration on the pulmonary artery cannula (PE 240 tubing), which is filled with contrast and is of a known diameter. For calibration, the average diameter from 20 slices was used to determine the calibration factor. Diameter estimation entailed 2 steps, plane extraction (Figure 10A) followed by a model fit algorithm (Figure 10B) as described below. Because this measurement technique uses gray scale data and is hybrid method based on a combination of FWHM and BAP, it is effective throughout the entire vascular tree and avoids difficulties, caused by factors such as partial volume effects and vessels that are smaller than the PSF, often seen with other diameter estimation routines.

i. Plane extraction: To extract 2D slices at discrete locations throughout the vascular network a direction vector, which is a local approximation of the vessel's medial axis is created by joining consecutive points along the skeletonized medial axis pathway data. An AVW function call, 'AVW_MakeMatrixFromAxis', was used to generate a 2D plane approximately orthogonal to and centered on the point identified on the medial axis. To ensure that the data in the selected plane contained an accurate representation of vessels' cross-section (using the well known fact that pulmonary arteries are typically circular in cross-section), we further improved the plane's orthogonality by creating a set of vectors extending from the center of the plane to a region distally along and surrounding the medial axis. The range of this region was simply defined by medial axis and the 8 voxels in the neighborhood surrounding it, at a distance 5 voxels downstream from the data plane. Oblique planes were extracted using the nine vectors to obtain individual cross-sections, each with a normal vector slight tilted away from the medial axis.


For each oblique plane, the central vessel cross-section was isolated using AVW's seeded region-growing procedure initiated at the central pixel, which also coincides with the vessel's medial axis and by default is a well-defined estimate of the center of the vessel. The threshold for this segmentation was that previously used for global tree segmentation. The segmented vessel cross-section extracted from each plane was then checked for its circularity index (CI), defined as the ratio of its squared perimeter (P) to its area (A), see Equation 1, using the AVW function call, 'AVW_ComputeCircularity'.

$$CI = \frac{P^2}{A} \quad \text{Equation 1}$$

Data from the plane with the most circular vessel cross-section was then used in diameter estimation. If the CI from all 9 orientations was not within ± 2.0 of the CI of a perfect circle, that slice was not used for diameter estimation and the algorithm indexed to the next point along the medial axis. Measurement planes extracted near bifurcations along the pulmonary vascular tree often exceed the threshold chosen for the circularity index and are rejected since the vessel cross-section in such planes resemble ellipses or other complex shapes.

ii. Vessel fitting and diameter estimation: Once the appropriate 2-D plane had been selected, it was fit to a MGF, by a process of two-stage numeric optimization described previously by Karau et al. [4]. The diameter estimation was performed using a technique of multidimensional, constrained non-linear least squares fitting. A variant of the Levenberg-Marquardt least squares

minimization implemented by Manolis Lourakis [24], was used under the terms of the GNU General Public License[25]. The iterative technique optimized parameters descriptive of the structure of the MGF, the functional form represented mathematically in Equation 2, and schematically by the adjoining insert.

$$F(x) = \frac{G_{SN_m} (G_{\max} - G_{SN_m}) e^{x^2 k a^2 / 2}}{G_{SN_m} (G_{\max} - G_{SN_m})} \dots x(k a)$$


Insert: Modified Gaussian Function

Equation 2

The parameters below were then used in the optimized fitting to Equation 2:

1. a , the plateau region of the MGF, the portion of the vessel between $(k-a)$ and $(k+a)$, where the attenuation from the contrast agent is fairly uniform.
2. σ , the roll-off of the MGF or Modified Gaussian Surface (MGS, when rotated over 360 degrees) and reflects the standard deviation of the Point Spread Function (PSF), the boundary at the vessel edges.
3. G_{\max} , the maximum of the MGF(S), an average GSN in the lumen of the vessel.
4. GSN_m , the minimum of the MGF(S), the image background.
5. $[h,k]$: the coordinates for center of the vessel cross-section. h is introduced for the second fitting iteration in which the entire plane of data is used.

Line-scan fit (stage-one): Fitting starts with default initial guesses for the 5 parameters, where a one-dimensional (1-D) procedure fits an averaged line-scan, see Figure 11, to provide a set of updated initial guesses for a subsequent 2-D surface fit. The default initial guesses, which were determined for a representative cannula cross-section intensity profile, were typically only used for the fitting of the cannula for the calibration step described above. Subsequently, the initial guesses for 1-D fitting were those resulting from the previous 2-D fitting. If the maximum number of iterations (N=1000) for the fitting procedure was reached without convergence, the initial guesses were set to the original initial guess for the cannula. If the fitting procedure still failed to converge, measurement at this location was abandoned and the process was restarted at the next point along the medial axis. The line-scan used in the initial fit was generated autonomously within the algorithm by averaging two perpendicular (horizontal and vertical) lines of data intersecting at the mid-point of the selected plane, see Figure 12A. Prior to performing the 1-D fitting, the original vessel orientation, which assumes the center of the vessel is located along the medial axis, is finely adjusted by finding the centroid of the vessel cross-section using AVW function 'AVW_ComputeImageCentroid' and then translating the data in the plane to align the centroid to the center of the plane. Because the orientation is forced in this manner, the estimate for the center of the vessel is simply the mid-point of the line-scan. Given the morphological characteristics of the rat arterial tree, such as its monopodial structure and typical branching angle, it is rare that a substantial vessel or object will be included in the lines of data used to determine the averaged line-scan. An exception to this is shown in Figures 11 & 12. In this case, the fitted parameters will not be optimized for the vessel of interest, however, the estimate of GSN_m is important and necessary for reassigning voxel values in the masking procedure and the rest of the estimated parameter values are still reasonable approximations for the second-stage of the fitting procedure.

Plane masking: The masking procedure was designed to extract adjacent vessels and minimize the effects caused by data extraneous to the central vessel under examination. This was accomplished by reassigning voxel values in regions of the selected plane, which include features such as vessels or airways, that would otherwise reduce the accuracy and/or convergence of the Levenberg-Marquardt fitting procedure. AVW_ConnectAndKeepImage was used to identify and isolate the central vessel under examination by reassigning the value of every voxel, that had a value above a threshold (the value used previously as a global threshold) and additionally was not connected to the central vessel, to GSN_m , which was estimated from the initial 1-D fitting. An example of this masking is seen in Figure 12B.

2-D surface fit (stage-two): Data from the entire masked plane was fit to a Modified Gaussian Surface (MGS), created by using the updated initial guesses and a spatially rotated MGF, to determine the final optimized parameters describing the structure of the vessel cross-section in terms of the MGF (Figure 13). The incidence of convergence for the 2-D fit was very high. In the rare case of non-convergence, the algorithm first attempted to refit the vessel using the default initial guesses for the cannula and if the fitter still did not converge, it aborted the measurement and indexed to the next point along the medial axis.

Diameter estimation: Vessel diameters were then calculated using:

$$D = \frac{A}{s \left(1 - \frac{GSN_m}{GSN_{max}} \right)} \quad \text{Equation 3,}$$

where D is diameter, A is the area under the MGS and s is the slope of the area-diameter line when $GSN_m = 0$ and GSN_{max} is the maximum GSN for the entire image volume. The value of s was determined during the cannula calibration using Equation 4.

$$s = \frac{1}{\frac{D_t}{A_c} \left(1 - \frac{GSN_m}{GSN_{max}} \right)} \quad \text{Equation 4,}$$

where D_t is the known diameter of the cannula and A_c is the measured cannula area. The diameter and 3-D coordinates of the location of measurement plane and vessel are recorded for further analysis and review. Vessel diameter estimation was repeated at each set of coordinates identified along the length of the selected vascular path with the initial guesses for the 5 parameters used in the subsequent 1-D fitting being updated to those resulting from the current 2-D fitting result.

Validation

The AVDMA code was validated by comparing the results to those generated by the operator guided manual technique (OGMT) for the same data. The accuracy of the OGMT technique and the MGF fitting protocol was previously validated over a range of diameters using a phantom as a gold standard[4]. In this study, micro-CT datasets of pulmonary arterial tree structures of rats exposed to CH (10% O₂ for 21 days, N = 4) and normoxia (21% O₂ for 21 days, N = 4) were analyzed. The AVDMA took an average of 5.25 hours to process a set of 4 reconstructions (497³ pixels) of the lung (one at each intravascular pressure) on a 1200 MHz AMD Athlon processor, 1 GB RAM, compiled by gcc version 4.1.1 and using the Debian Woody GNU/Linux version 2.4.24 operating system. For comparison, the OGMT of the same data takes approximately 30 hours of intense user interaction. Validation between OGMT and AVDMA methods was carried out by performing a normalized root mean squared error

(NRMSE) calculation between diameters estimated by OGMT versus ADVMA as well as statistical tests on model based parametric results from each method.

The efficacy of the AVDMA is apparent in plot of vessel diameter as a function of distance from the inlet (Figure 14A). In these plots, distance is calculated as the cumulative path length of the main trunk calculated using Matlab (MathWorks, Natick, MA) by applying point-to-point 3-D Euclidean distance referenced to the inlet location. Since small deviations in the ideal path accumulate, path length is dependent on the number of sample points along the path. Therefore, to provide a more valid comparison, we have reduced the automated data to contain only the number of points (those found in the same proximity) as in the manually measured data. A simple closest 3-D proximity algorithm identified one-to-one point matching and the cumulative trunk length for the sub-sampled data was recalculated, see Figure 14B. A statistical comparison between sub-sampled AVDMA and OGMT data from all rats in the study showed the average NRMSE was less than 5%. NRMSE was calculated as root mean squared error (RMSE) divided by the range of the observed vessels diameters. For error data from all rats at each intravascular pressure, see Table 1. Figures 14C and 14D present pulmonary arterial diameter-distance curves for data obtained from the AVDMA and manual methods for a Sprague-Dawley Control (SDC) lung imaged at four intravascular pressures with.

A statistically significant difference between morphometric parameters, such as arterial distensibility has been shown between Sprague-Dawley control SDC and CH (SDH) lungs [7]. Similar morphological changes are illustrated by the differences seen between a SDC and SDH rat analyzed with the AVDMA protocol as shown in Figures 14E and 14F. SDH lungs tend to have smaller luminal diameters and shorter overall main trunks, an observation made in previous studies and quantitatively validated using AVDMA data and parametric analysis in this study.

Parametric analysis

The diameter-distance relationship along the arterial main trunk has been parameterized in terms of Equation 5 in an earlier study by Karau et al. [23].

$$D(x) = D(0) \left(1 - \frac{x}{L_{tot}}\right)^c$$

Equation 5.

where, for a fixed intravascular pressure, $D(0)$ is the approximate luminal diameter at the inlet ($x = 0$), L_{tot} is the projected length of the main trunk when the diameter of the vessel equals zero ($D = 0$) and c is a measure of the taper of the main trunk. Models have been developed that incorporate arterial distensibility to better understand the behavior of the principal pathway and the main trunk at the different intravascular pressures [4, 22]. This study integrated two distinct models for the statistical validation of the AVDMA, and applied arterial distensibility as the primary investigative parameter.

Two techniques were used to estimate the distensibility (α) of the pulmonary vascular tree. The first, a multi-parameter surface fit technique, applied unconstrained multi-variable non-linear optimization to simultaneously fit the diameter-distance data from the four arterial pressures. The second technique was based on individual vessel segment distensibility and calculated the arterial distensibilities of individual vessel segments. Previous work {Molthen, 2004 #48; Karau, 2001 #2} has shown that $D(0)$ vs. β in rat lungs was diameter independent and therefore α can be used to represent a unique distensibility for the entire pulmonary tree [4, 22].

Equation 6 describes vessel diameter over a range of pressures and as a function of distance from the inlet. This relationship has been derived using the well-documented relation between luminal diameter and pressure [26-28].

$$D(x, P) = D(0, 0) (1 + \alpha P)^c \left(1 - \frac{x}{L_{tot}}\right)^c \quad \text{Equation 6,}$$

where α is a distensibility coefficient representing the entire vascular tree. Combining Equations 5 and 7, we have,

$$D(x, P) = D(0, 0) (1 + \alpha P)^c \left(1 - \frac{x}{L_{tot}}\right)^c \quad \text{Equation 7.}$$

$D(0, 0)$, x , L_{tot} and α can be estimated by fitting the data to the model described by Equation 7. To accomplish this an unconstrained multivariable non-linear optimization was performed using the Matlab function 'fminunc' in the Optimization toolbox. Figure 15 shows OGMT and AVDMA data fit to the model (surface). The OGMT, sub-sampled AVDMA, and full AVDMA data sets were fit to the model and results are presented in Table 2. For each method of measurement, the path length (L_{tot}) and arterial distensibility (α) exhibited statistically significant differences (t-test; $p < 0.05$) between the control and CH data sets, consistent with the previously published results using the OGMT data [22]. The vessel undistended diameter (D_0) also tended to be small in the CH lungs. These results reflect the PVREM occurring in the pulmonary arteries in the CH rats. The arteries throughout the tree are stiffer and less distensible. The effective length of the pulmonary trunk shortens because of encroachment on the lumen of the small arteries as well as the loss in compliance that causes a lack of filling in the distal vessels for equivalent intravascular pressures. The taper along the main arterial trunk (c) is not significantly difference between the two experiment groups. Although we may expect a change in this parameter, the results would also indicate that the luminal diameter change is independent of vessel diameter.

An alternative method of calculating pulmonary tree α is to directly apply the pressure vs. diameter relationship in Equation 8 forwarded by Yen et al. [28].

$$D(P) = \beta P + D(0) \quad \text{Equation 8,}$$

where $D(P)$ is the luminal diameter for a particular vessel segment at arterial pressure P (which is the localized intravascular pressure in mmHg), $D(0)$ is the diameter at $P = 0$, and β is the distensibility coefficient for individual vessel segments. We used Equation 8 to estimate $D(0)$ and β by fitting data from the sub-sampled individual vessel segments in an example SDC rat measured by the AVDMA at the four intravascular pressures (Figure 16A). Since we have found the pulmonary artery distensibility to be independent on vessel diameter in our rat models, i.e., a linear regression of $D(0)$ vs. β has an intercept which is not significantly different from zero, we use an estimate of the slope of the $D(0)$ vs. β relationship as an approximation of α , again a parameter estimating arterial distensibility for the entire lung. $D(0)$ vs. β for each vessel segment measured in an example lung are plotted in Figure 16B. One line in Figure 16B represents the linear regression of the data and the other a linear regression where the intercept has been forced to zero. Columns titled Individual Vessel Fit in Table 3 reports α estimated as the slope of the regression line with a zero intercept, represented mathematically in Equation 9.

$$\alpha = \frac{\beta}{D(0)}$$

Equation 9.

It is important to note that the arterial distensibility calculated in this fashion requires the identification and measurement of the same portion of each individual vessel segment in each pressure data set. Therefore, only sub-sampled AVDMA data could be used for this analysis, assuming each measurement's proximity to the OGMT mapped points insured repeated measurements at the same location. $D(0)$ vs. β relationships for an example SDC and SDH lung are presented in Figure 16C for AVDMA measured data. The results of calculating α from AVDMA data for the 8 rats are summarized in the second and third column of Table 3. There was no statistical difference (t-test; $p > 0.05$) in α calculated either through multi-parameter fitting using Equation 7 or individual vessel distensibility using Equation 9. Further analysis comparing α estimated using the individual vessel fit to OGMT data is presented in the forth column of Table 3. Each method confirms a difference in pulmonary arterial distensibility between SDC and SDH rats.

Discussion and Conclusion

AVDMA is a tool to extend our previous work [4,22,23], and has been designed to bring about a more comprehensive, detailed, efficient, and consistent analysis, as well as provide a significant reduction in effort and time required by persons performing the analysis. The AVDMA method comprehensively and effectively maps and measures the pulmonary tree from the large pulmonary artery inlet down to distal vessels tens of microns in diameter. The time required for data analysis is significantly reduced using the AVDMA. For example, on the same computer time of analysis for a single lung data set with 4 intravascular pressures is reduced from 25-35 hours using the OGMT method (in which user interaction is continuously required) to approximately 5 hours (with minimal user interaction, approximately 10-15 minutes is required to specify input files, scan geometry, and identify two locations along the main arterial trunk) for the AVDMA method.

In our protocol, operators examined and confirmed the validity and consistency of data produced by the AVDMA. In our experience, non-convergence of the Levenberg-Marquardt fitter was rare and no significant data was missing from main trunk except around bifurcations, which was expected and resulted primarily from the algorithm rejecting non-circular object profiles that occur in these regions. A factor that likely contributes to the success of the vessel fitting is the geometry of the pulmonary arterial tree. During the process of extracting small planes of data orthogonal to the medial axis of a vessel under examination, the inherent structure of the tree makes it improbable that the plane will contain any significant portion of another vessel of similar or larger size that will cause the fitting algorithm to struggle because of multi-minima due to adjacent objects. We have further addressed this issue by minimizing the effects of extrinsic adjacent objects, first by reducing the probability of including any, i.e., sampling only one vertical and one horizontal line of data from the plane for first-stage 1-D fitting, secondly by averaging two lines before performing the 1-D fit, and finally by masking out all significant objects other than the central vessel in the plane before performing the final second-stage 2-D surface fit. Even though the occurrence of adjacent objects in our data is fairly rare, we have highlighted an example of a case (Figures 11 & 12) where the AVDMA has managed an extrinsic object successfully.

The results from the OGMT and AVDMA techniques were fundamentally the same. The average normalized root mean squared error (NRMSE) for all the data was below 5%. It is important to note that the estimated errors calculated are over estimates since it is not guaranteed

that the most distal pathway defined by the adaptive thresholding algorithm always coincides directly with the pathway that was identified by the OGMT method. Therefore, our calculations of NRMSE inevitably include comparison of similar but different vessels in the most distal portion of the main trunk.

The AVDMA measured many more points along the main trunk compared to OGMT. This higher sampling density resulted in an estimated cumulative trunk length closer to the true length of the trunk. This effect can be seen in Figure 13 and in the L_{tot} data in Table 2. The difference in path length between the two techniques can be better understood by observing the schematic in Figure 17, which demonstrated the fact that the geometric length of an arc is longer than the equivalent chord and that higher sampling will result in the AVDMA mapping a more tortuous path. The increased sampling density also produces an enhanced representation of vessel morphology, since individual vessel segments are measured all along their length, as opposed to only at a single location at the midpoint, as in the OGMT technique. Thus, the AVDMA allows investigation of variations in diameter along the length of individual vessel segments, enabling further insight into hemodynamic characteristics between bifurcations. We have observed a convexity in vessel segments that is decreased in the presence of CH exposure and PH, data not shown. In addition, we have also used the AVDMA to successfully differentiate between SDC and SDH rat lungs showing a decrease in vessel distensibility in SDH rats. These decreases could have significant implications in the role that these arteries play in pulse dampening, pulmonary pulse pressure and the impedance seen by the right ventricle resulting in increased mortality in PH[29, 30].

We have presented data to illustrate the similarities in the morphological characteristics of the diameter-distance relationship as calculated by the OGMT and AVDMA methods. Arterial distensibility (α) calculated using either the multiparameter morphometric model fit or the individual vessel segment distensibility method provided comparable results and differences in α between the SDC and SDH lungs were consistent, independent of the measurement method used.

The primary objective of the AVDMA study was the creation of an automated alternative to the morphological analysis procedure utilized by our group [4,22,31]. While the AVDMA has demonstrated significant advantages, such as improved consistency, minimized user interaction and much higher throughput, certain issues need to be addressed before the method is fully autonomous. For instance, the OGMT mapping procedure was confined to identification of vessel segments defined by the principal pathway, to implement a data reduction scheme that uses the concept of self-consistency within the pulmonary vascular structure. By definition, the principal pathway is comprised of the main arterial trunk and its immediate branches or daughter branches[23]. Although it is straight forward for the AVDMA to map and measure the entire vascular tree, it requires operator guidance to identify and compare unique portions of the tree from one lung to the next. The current AVDMA has been designed to map and measure operator-identified vascular pathways and was used specifically to quantify the main arterial trunk. Future development of the AVDMA will incorporate automated quantification of multiple vascular pathways while supporting accurate registration of vessel segments for repeated measures at different intravascular pressures. Ongoing efforts by our group are underway to investigate an accurate identification and classification technique for the common individual vessel segments, which would facilitate branch identification based on similar branching patterns and aid in appropriate registration protocols. This goal is challenging because of transformations in the vascular geometry, such as segment translation and partial or reduced filling that occur with changes in intravascular pressure. However having access to data from multiple vascular pathways and, in particular, to numerous small pulmonary vessel segments, will provide much needed data on the distal region of the vascular tree, considered to be the primary or more reactive and hemodynamically significant site of PVREM.

The AVDMA, while structured toward providing a detailed and consistent morphological analysis of pulmonary vascular structure, can easily be adapted for analyzing vasculature from different anatomical sites, such as the heart, kidney, brain, etc. The basic algorithm can be used as a more general research tool by implementing moderate modifications. Because of higher throughput, AVDMA based methods can enable faster, more in depth investigation into the etiology and progression of vascular diseases as well as to help identify the functional influences of vascular structure, consequently expediting research in the field of vascular biology.

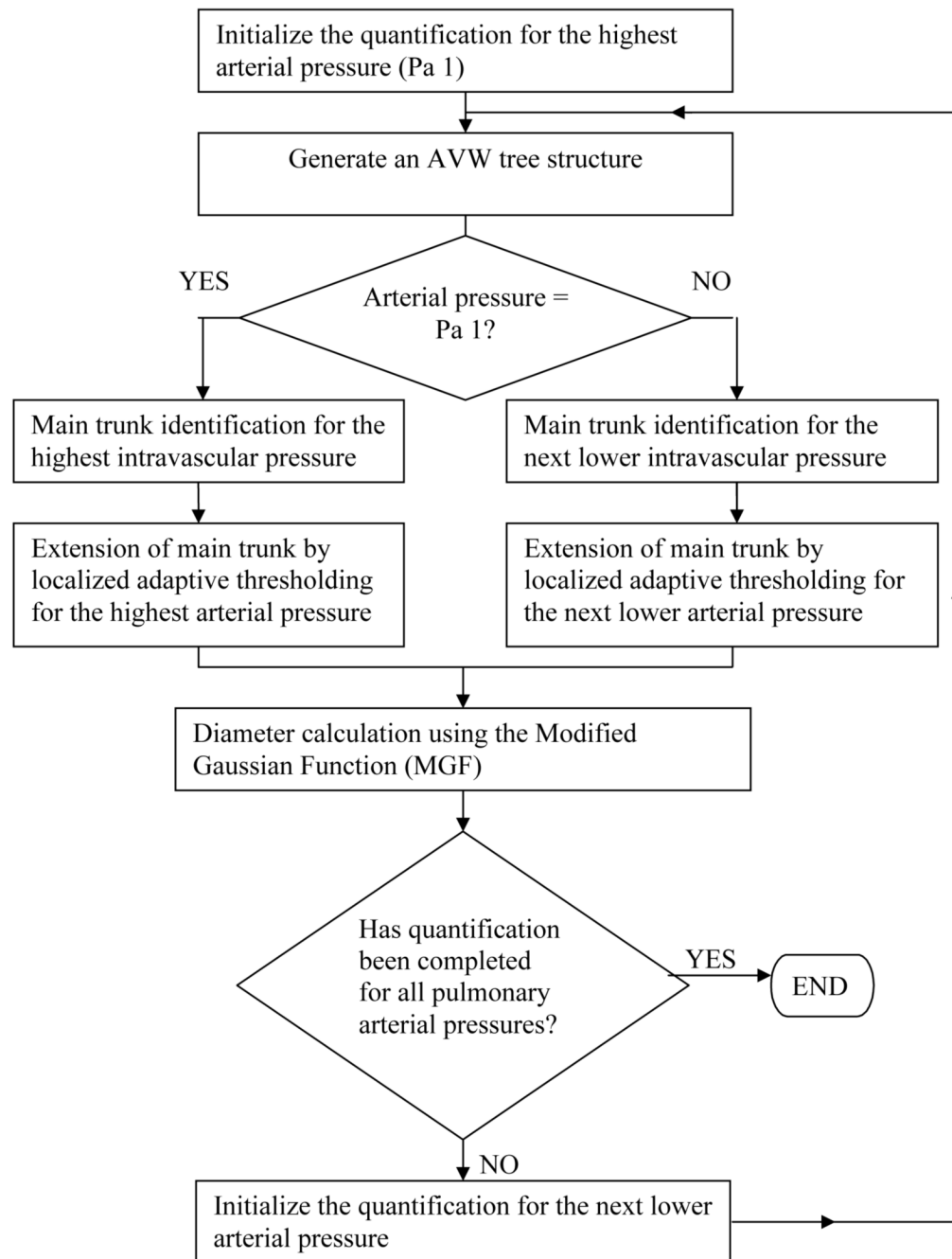
Acknowledgments

The authors would like to acknowledge funding from the Department of Veterans Affairs, NIH U19AI067734, and NIH HL 19298.

References

- [1]. Bradley WG. Radiology 2002: Near Term Advances in Medical Imaging. Medscape Radiology. 2001
- [2]. Bartling SH, Stiller W, Grasruck M, Schmidt B, Peschke P, Semmler W, Kiessling F. Retrospective motion gating in small animal CT of mice and rats. *Invest Radiol* 2007;42(10):704–14. [PubMed: 17984768]
- [3]. Hu J, Haworth ST, Molthen RC, Dawson CA. Dynamic small animal lung imaging via a postacquisition respiratory gating technique using micro-cone beam computed tomography. *Acad Radiol* 2004;11(9):961–70. [PubMed: 15350577]
- [4]. Karau KL, Johnson RH, Molthen RC, Dhyani AH, Haworth ST, Hanger CC, Roerig DL, Dawson CA. Microfocal X-ray CT imaging and pulmonary arterial distensibility in excised rat lungs. *American Journal of Physiology - Heart and Circulatory Physiology* 2001;281(3):H1447–H1457.
- [5]. Grosskopf, S.; Biermann, C.; Deng, K.; Chen, Y. Medical Imaging 2009: Image Processing. SPIE; Lake Buena Vista, FL, USA: 2009. Accurate, fast, and robust vessel contour segmentation of CTA using an adaptive self-learning edge model; p. 72594D-8.
- [6]. Kawajiri, S.; Zhou, X.; Zhang, X.; Hara, T.; Fujita, H.; Yokoyama, R.; Kondo, H.; Kanematsu, M.; Hoshi, H. Medical Imaging 2007: Image Processing. SPIE; San Diego, CA, USA: 2007. Automated segmentation of hepatic vessel trees in non-contrast x-ray CT images; p. 65123A-8.
- [7]. Kubassova O. Automatic segmentation of blood vessels from dynamic MRI datasets. *Med Image Comput Comput Assist Interv Int Conf Med Image Comput Comput Assist Interv* 2007;10(Pt 1): 593–600.
- [8]. Lee J, Beighley P, Ritman E, Smith N. Automatic segmentation of 3D micro-CT coronary vascular images. *Med Image Anal* 2007;11(6):630–47. [PubMed: 17827050]
- [9]. Lobregt S, Verbeek PW, Groen FCA. Three-dimensional skeletonization: Principle and algorithm. *IEEE Transactions on Pattern Analysis and Machine Intelligence* 1980;PAMI-2(1):75–77.
- [10]. Lorenz, C.; Lessick, J.; Lavi, G.; Bulow, T.; Renisch, S. Medical Imaging 2004: Image Processing. SPIE; San Diego, CA, USA: 2004. Fast automatic delineation of cardiac volume of interest in MSCT images; p. 456-466.
- [11]. Lorenz, C.; Renisch, S.; Schlathoelter, T.; Buelow, T. Medical Imaging 2003: Physiology and Function: Methods, Systems, and Applications. SPIE; San Diego, CA, USA: 2003. Simultaneous segmentation and tree reconstruction of the coronary arteries in MSCT images; p. 167-177.
- [12]. Zhou C, Chan HP, Sahiner B, Hadjiiski LM, Chughtai A, Patel S, Wei J, Ge J, Cascade PN, Kazerooni EA. Automatic multiscale enhancement and segmentation of pulmonary vessels in CT pulmonary angiography images for CAD applications. *Med Phys* 2007;34(12):4567–77. [PubMed: 18196782]
- [13]. Bruyninckx, P.; Loeckx, D.; Vandermeulen, D.; Suetens, P. Medical Imaging 2009: Image Processing. SPIE; Lake Buena Vista, FL, USA: 2009. Segmentation of lung vessel trees by global optimization; p. 725912-12.

- [14]. Buelow, T.; Wiemker, R.; Blaffert, T.; Lorenz, C.; Renisch, S. Medical Imaging 2005: Physiology, Function, and Structure from Medical Images. SPIE; San Diego, CA, USA: 2005. Automatic extraction of the pulmonary artery tree from multi-slice CT data; p. 730-740.
- [15]. Kaftan, JN.; Kiraly, AP.; Bakai, A.; Das, M.; Novak, CL.; Aach, T. Medical Imaging 2008: Image Processing. SPIE; San Diego, CA, USA: 2008. Fuzzy pulmonary vessel segmentation in contrast enhanced CT data; p. 69141Q-12.
- [16]. Raghupathi, L.; Lakare, S. Medical Imaging 2009: Computer-Aided Diagnosis. SPIE; Lake Buena Vista, FL, USA: 2009. A hybrid lung and vessel segmentation algorithm for computer aided detection of pulmonary embolism; p. 726033-10.
- [17]. Zhou, C.; Chan, H-P.; Hadjiiski, LM.; Patel, S.; Cascade, PN.; Sahiner, B.; Wei, J.; Ge, J.; Kazerooni, EA. Medical Imaging 2006: Image Processing. SPIE; San Diego, CA, USA: 2006. Automatic pulmonary vessel segmentation in 3D computed tomographic pulmonary angiographic (CTPA) images; p. 61444Q-7.
- [18]. Robb RA, Hanson DP, Karwoski RA, Larson AG, Workman EL, Stacy MC. ANALYZE: a comprehensive, operator-interactive software package for multidimensional medical image display and analysis. *Computerized Medical Imaging and Graphics* 1989;13:433–454. [PubMed: 2688869]
- [19]. Robb RA, Barillot C. Interactive display and analysis of 3-D medical Images. *IEEE Transactions on Medical Imaging* 1989;8(3):217–226. [PubMed: 18230519]
- [20]. Robb RA. The biomedical imaging resource at Mayo Clinic. *IEEE Transactions on Medical Imaging* 2001;20(9):854–867. [PubMed: 11585203]
- [21]. Feldkamp LA, Davis LC, Kress JW. Practical cone-beam algorithm. *Journal of the Optical Society of America A* 1984;1:612–619.
- [22]. Molthen RC, Karau KL, Dawson CA. Quantitative models of the rat pulmonary arterial tree morphometry applied to hypoxia-induced arterial remodeling. *J Appl Physiol* 2004;97(6):2372–84. discussion 2354. [PubMed: 15333611]
- [23]. Karau KL, Molthen RC, Dhyani A, Haworth ST, Hanger CC, Roerig DL, Johnson RH, Dawson CA. Pulmonary arterial morphometry from microfocal X-ray computed tomography. *Am J Physiol Heart Circ Physiol* 2001;281(6):H2747–H2756. [PubMed: 11709444]
- [24]. Lourakis, MIA. levmar: Levenberg-Marquardt nonlinear least squares algorithms in C/C++. [accessed: January 2005]. <http://www.ics.forth.gr/~lourakis/levmar/2004>
- [25]. GNU General Public License. [accessed: January 2005]. [unspecifiedhttp://www.gnu.org/copyleft/gpl.html](http://www.gnu.org/copyleft/gpl.html)
- [26]. al-Tinawi A, Madden JA, Dawson CA, Linehan JH, Harder DR, Rickaby DA. Distensibility of small arteries of the dog lung. *J Appl Physiol* 1991;71:1714–1722. [PubMed: 1761466]
- [27]. Zhuang FY, Fung YC, Yen RT. Analysis of blood flow in cat's lung with detailed anatomical and elasticity data. *J Appl Physiol* 1983;55(4):1341–1348. [PubMed: 6629968]
- [28]. Yen RT, Fung YC, Bingham N. Elasticity of small pulmonary arteries in the cat. *J Biomech Eng* 1980;102(2):170–177. [PubMed: 7412241]
- [29]. Blyth KG, Syeed R, Chalmers J, Foster JE, Saba T, Naeije R, Melot C, Peacock AJ. Pulmonary arterial pulse pressure and mortality in pulmonary arterial hypertension. *Respir Med* 2007;101(12):2495–501. [PubMed: 17719764]
- [30]. Castelain V, Herve P, Lecarpentier Y, Duroux P, Simonneau G, Chemla D. Pulmonary artery pulse pressure and wave reflection in chronic pulmonary thromboembolism and primary pulmonary hypertension. *J Am Coll Cardiol* 2001;37(4):1085–92. [PubMed: 11263613]
- [31]. Karau KL, Molthen R, Johnson RH, Dawson C. Pulmonary arterial tree structure-function relationships from X-ray ct imaging. *Ann. Biomed. Eng* 2001;29:S136.

**Figure 1.**

Flowchart depicting the high-level process flow for the set of the AVDMA algorithms created to quantify the pulmonary vascular structure.

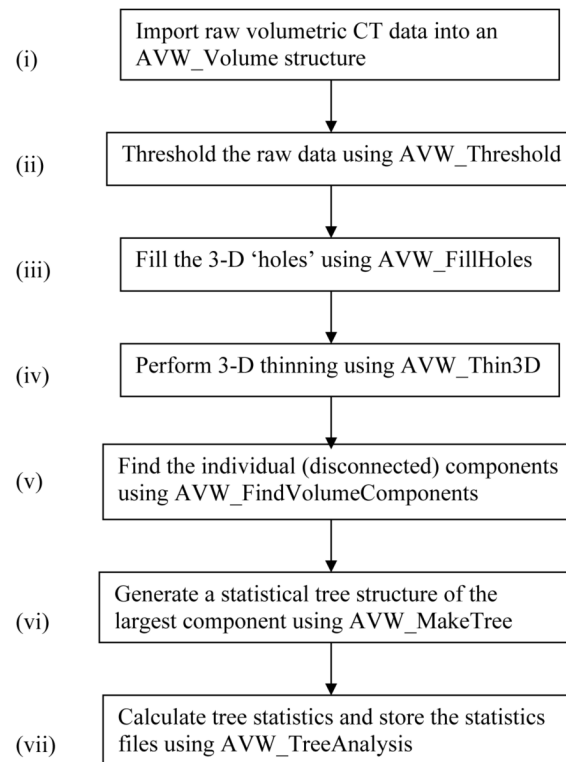


Figure 2.
Algorithm for the generation and subsequent analysis of a comprehensive AVW tree structure.

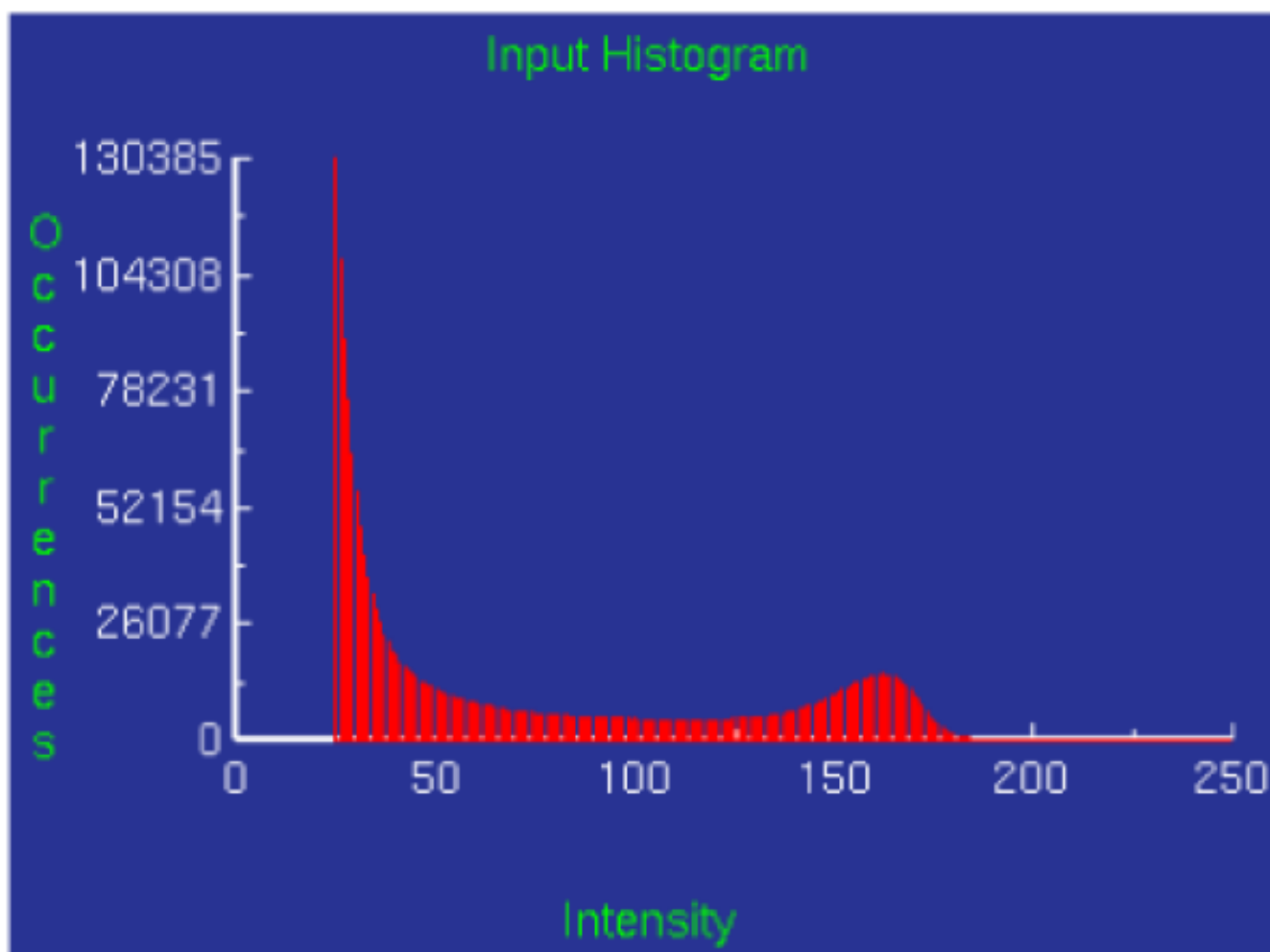


Figure 3. Histogram of a CT data volume from an example control rat lung with the rat pulmonary arterial tree filled with *perfluorooctyl bromide for X-ray contrast*.

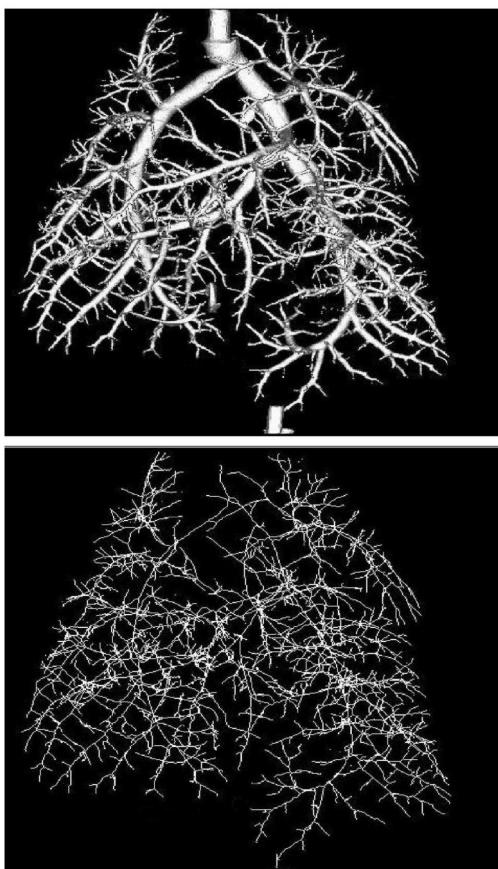


Figure 4.

Top: Gray scale volume Maximum Intensity Projection (MIP) renderings of the rat pulmonary arterial tree. Bottom: Skeletonization reduces the volumetric pulmonary vasculature to an approximation of its medial axis.

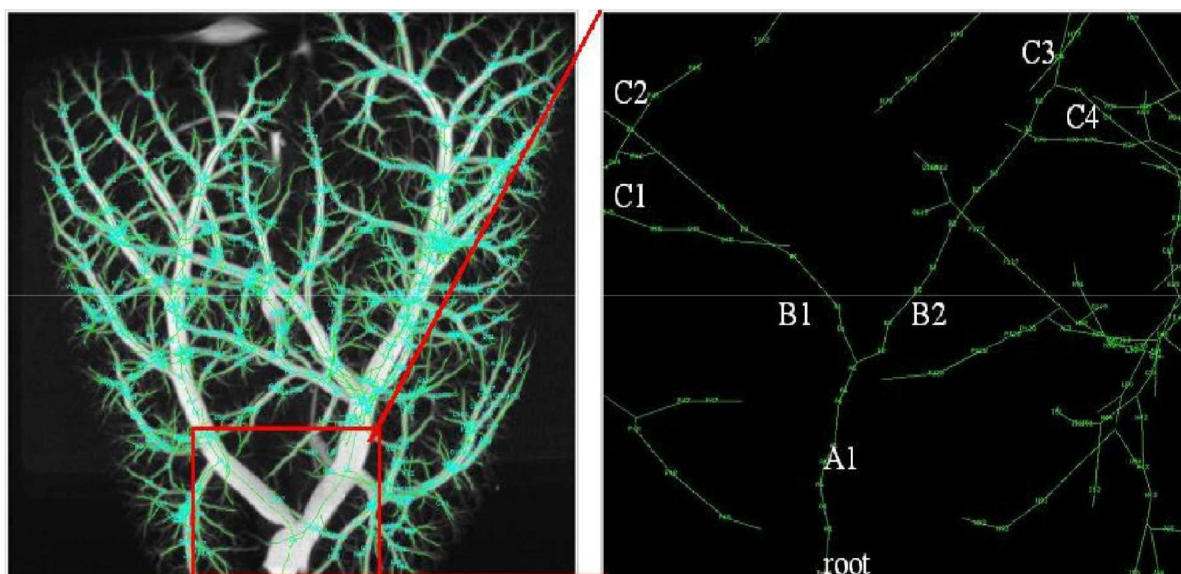


Figure 5.

Left: Skeletonization of tree (up-side-down to emphasize tree structure) superimposed with Maximum Intensity Projection (MIP). **Right:** Zoomed in ROI at left, depicting the base of the hierarchical mapping nomenclature starting at the root.

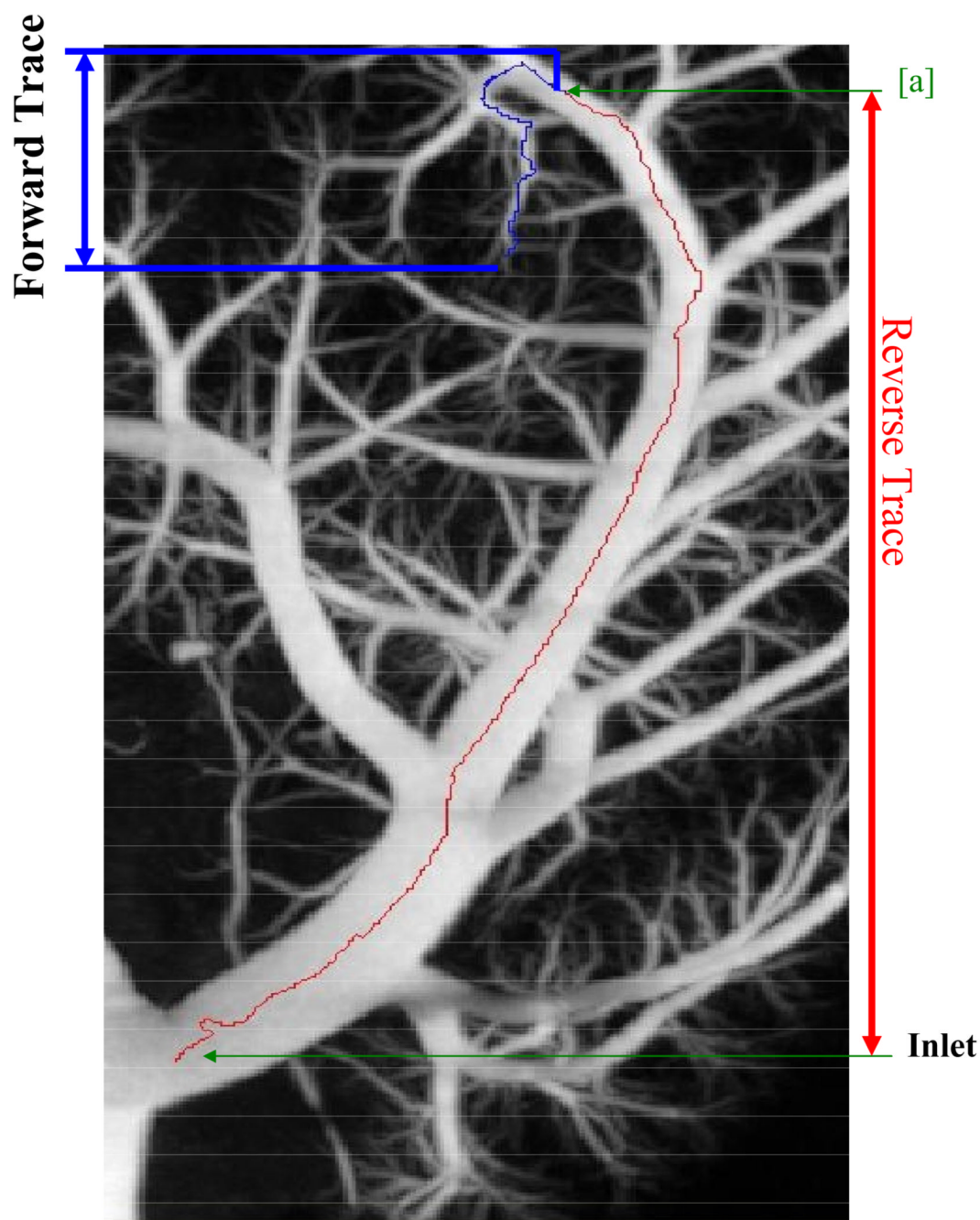
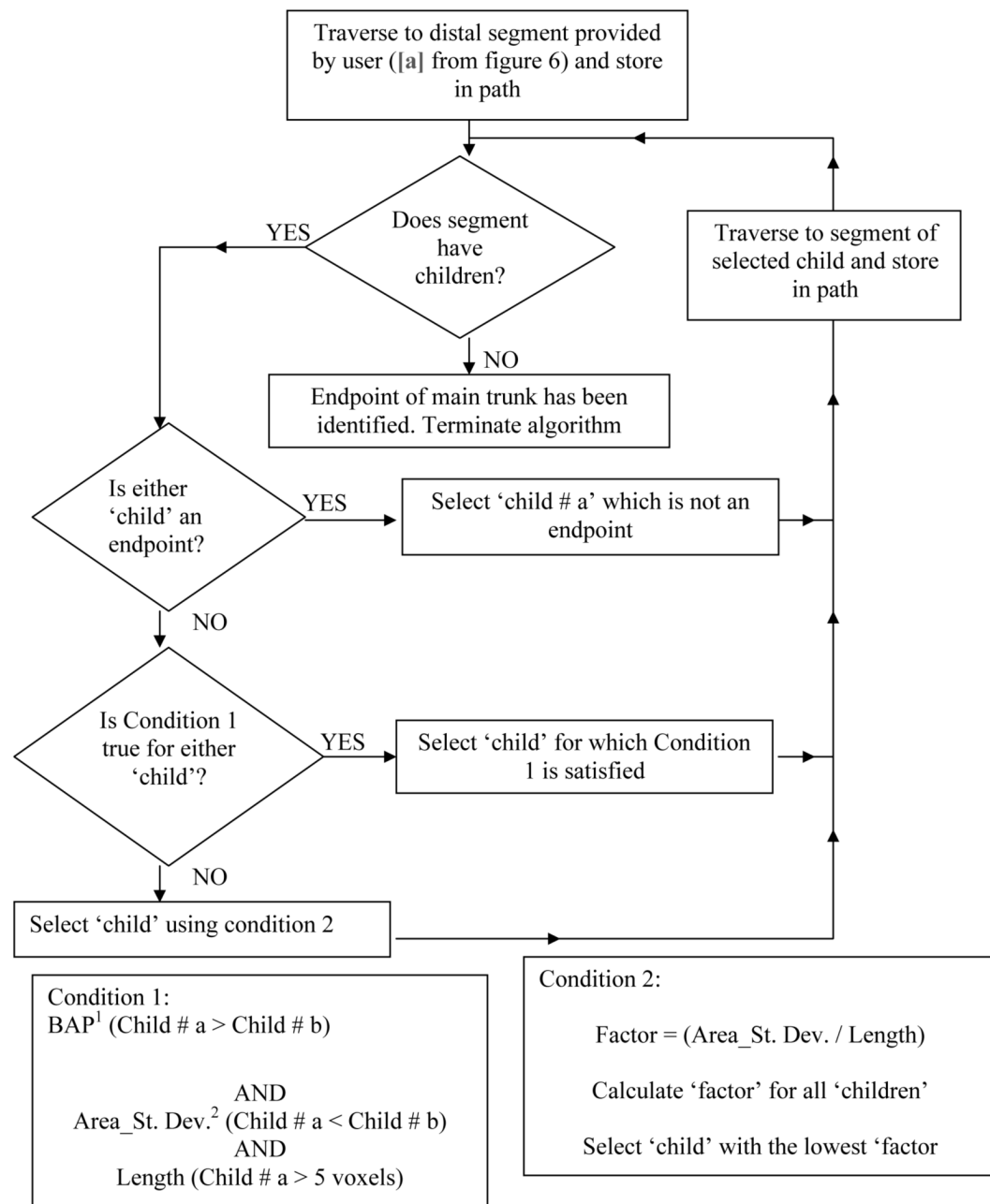


Figure 6. Tree rendering depicting the main trunk identification algorithm at the highest arterial pressure. The section of the main trunk from inlet to [a], is mapped using the reverse trace phase of the algorithm. Mapping continues in reverse from [a] to the terminus, with the forward trace phase of the algorithm.

**Figure 7.**

Algorithm describing the forward trace phase of the main trunk identification algorithm at the highest arterial pressure (Pa1). ¹BAP denotes Brightness Area Product; ²Area_St. Dev. denotes the vessel segment area standard deviation.

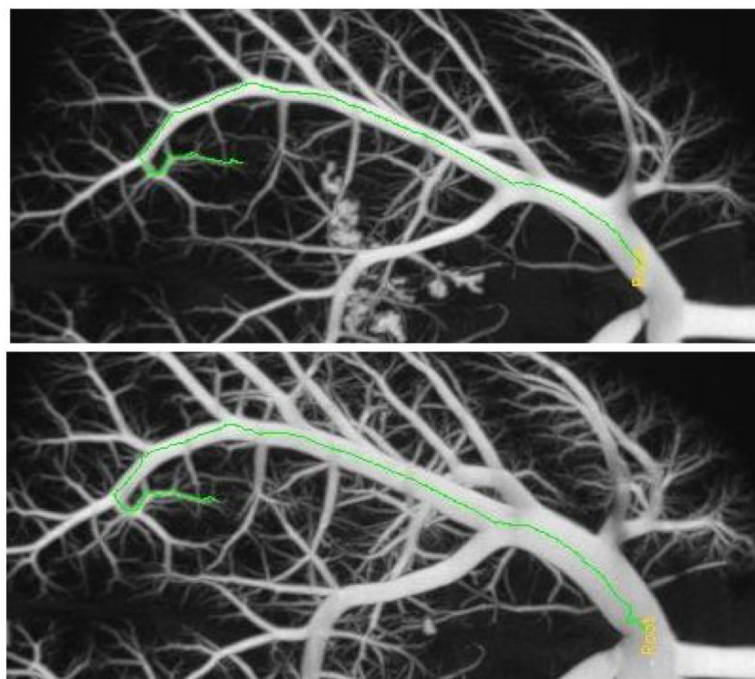


Figure 8. Renderings of the rat main pulmonary arterial trunk at intravascular pressures of 5.4 (top) and 30 (bottom) mmHg. The objective is to map the main trunk with identical vessel segments for all the pressures.

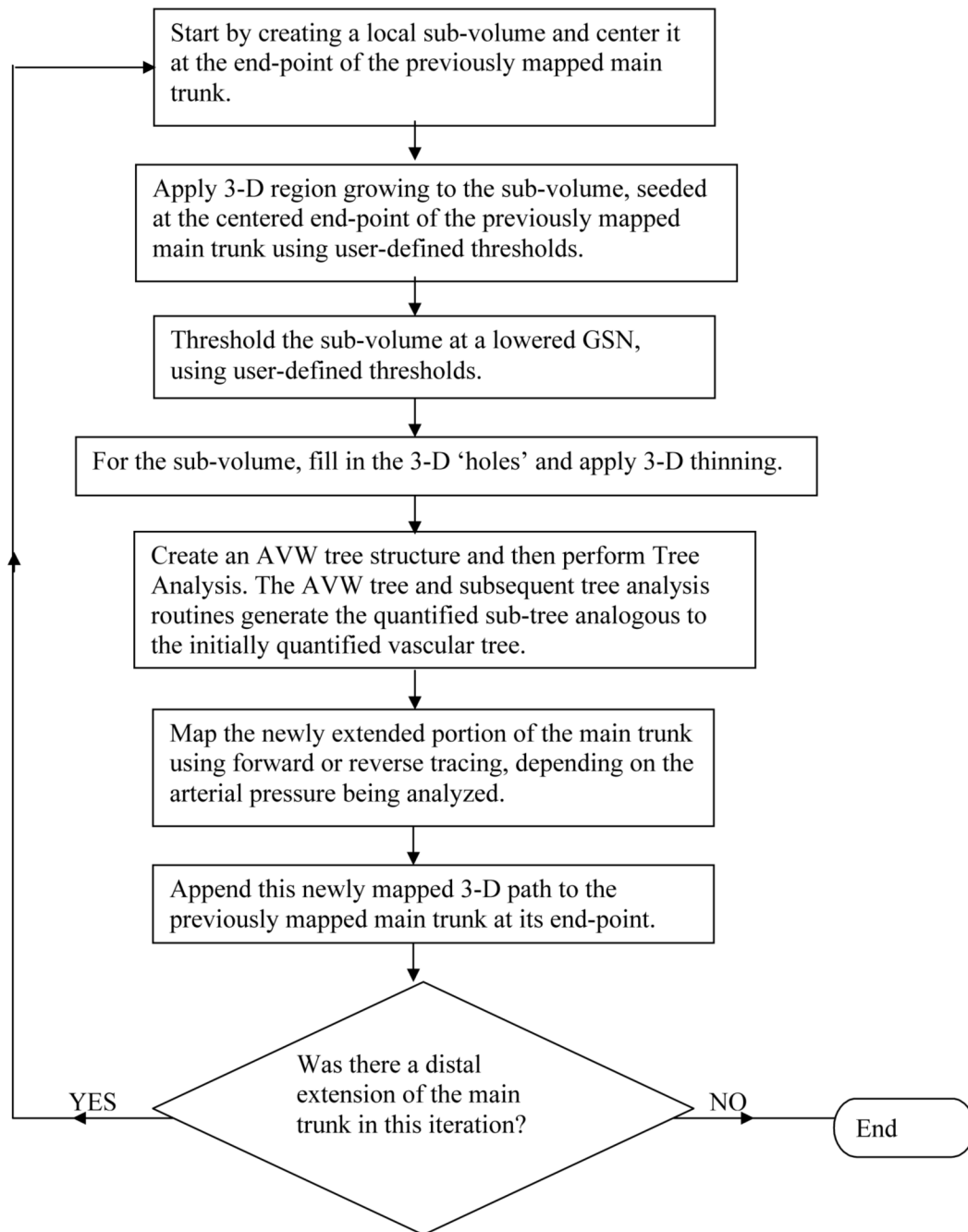
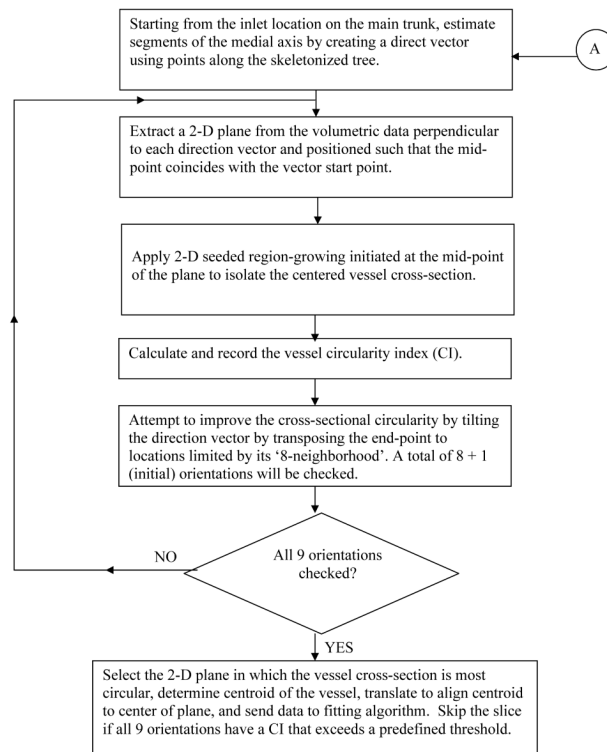
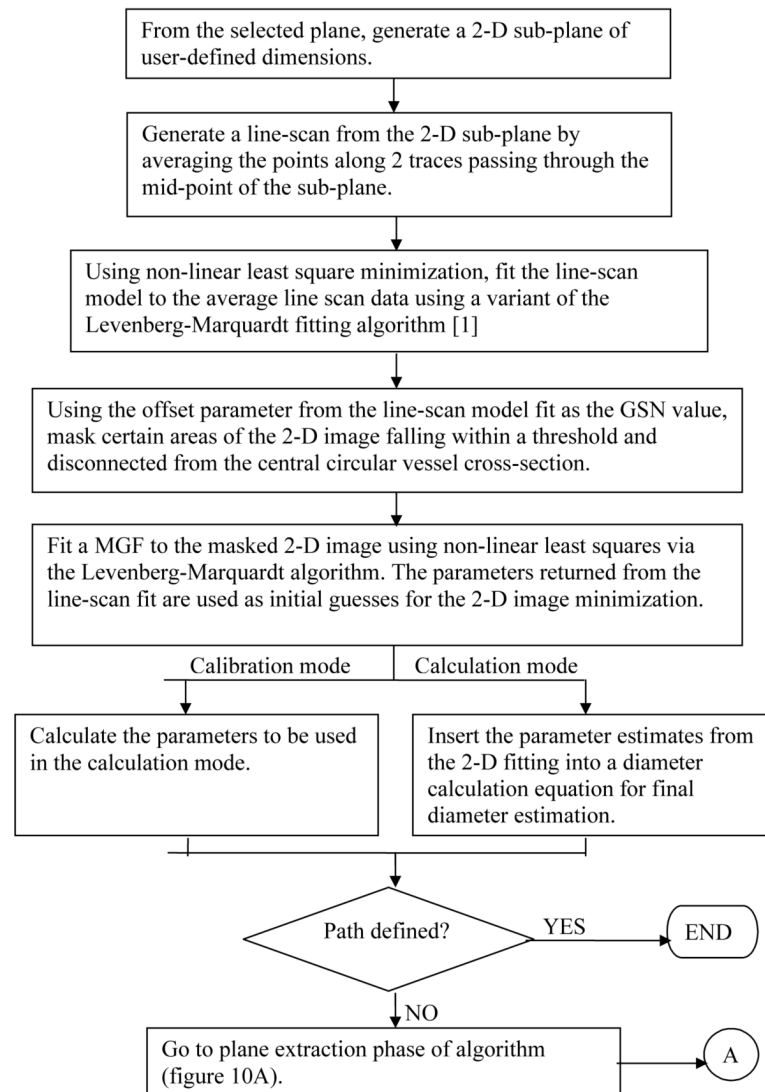


Figure 9.
Algorithm for adaptive thresholding.

A



B

**Figure 10A.**

Plane extraction phase of diameter estimation algorithm.

Figure 10B: Vessel fitting phase of diameter estimation algorithm.

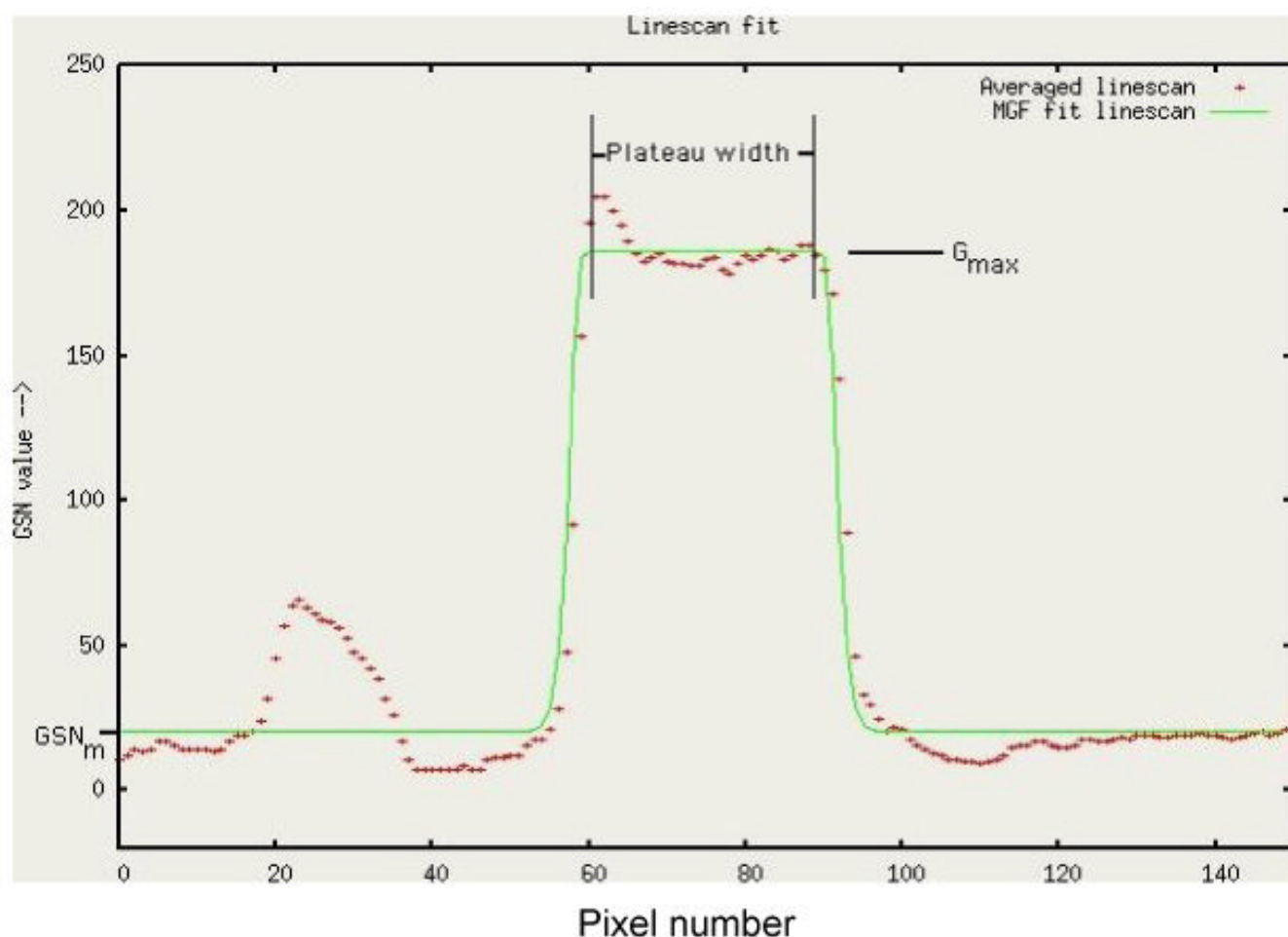


Figure 11.

Initial fit (solid line) of averaged line-scan data (+). The 2 lines in Figure 12A indicate the location of the 2 individual line-scans through the image's central row and column, that are selected to calculate the average line-scan. The spike in the averaged GSN value between pixels 20 and 40 is a result of the vertical line-scan intersecting another vessel (see lower half of the vertical line-scan in Figure 12A). The optimized values for width, G_{\max} (scale) and GSN_m (offset) have been indicated.

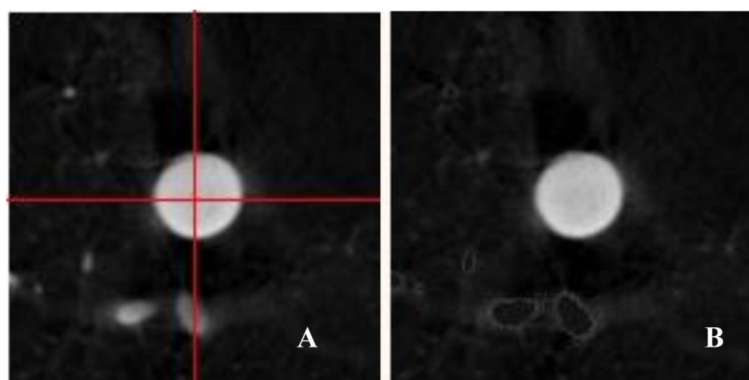


Figure 12.

Example of vascular masking operation. **A:** Original sub-plane selected diameter estimation. Lines indicate location of data used for initial fit iteration, see Figure 11. **B:** Data masked using the GSN_m (offset) estimated with the line-scan fit. The masking algorithm locates background voxels (disconnected from the central vessel cross-section) within user-defined intensities (GSN values) and replaces these voxel intensities with the GSN_m value. The background vessel, seen in Figure 12A, that caused a spike on the left side of the averaged line-scan (Figure 11) has been “masked” out, creating a smoothed image background.

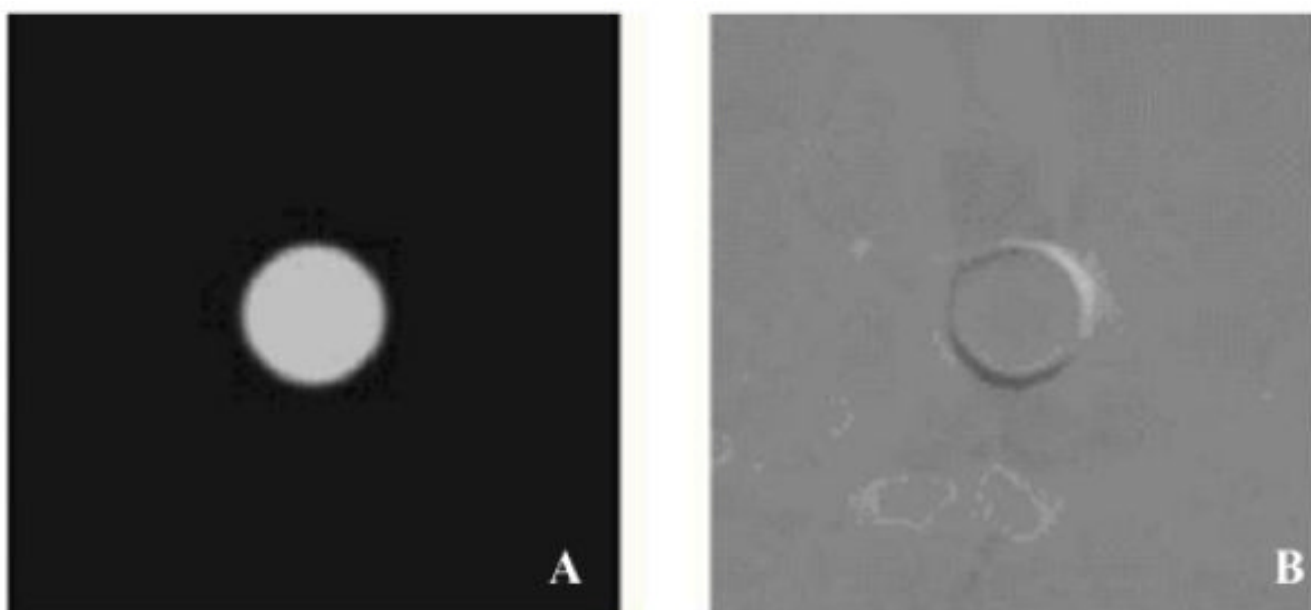


Figure 13.

2D images depicting the result of the non-linear least square minimization performed to estimate vessel diameters. **A:** 2D image of MGF model data generated using the optimized parameters resulting from fit to data in Figure 12B. **B:** The difference image resulting from subtracting the model data (A) and the original masked data (Figure 12B), rescaled to enable all values to fall within the positive GSN scale.

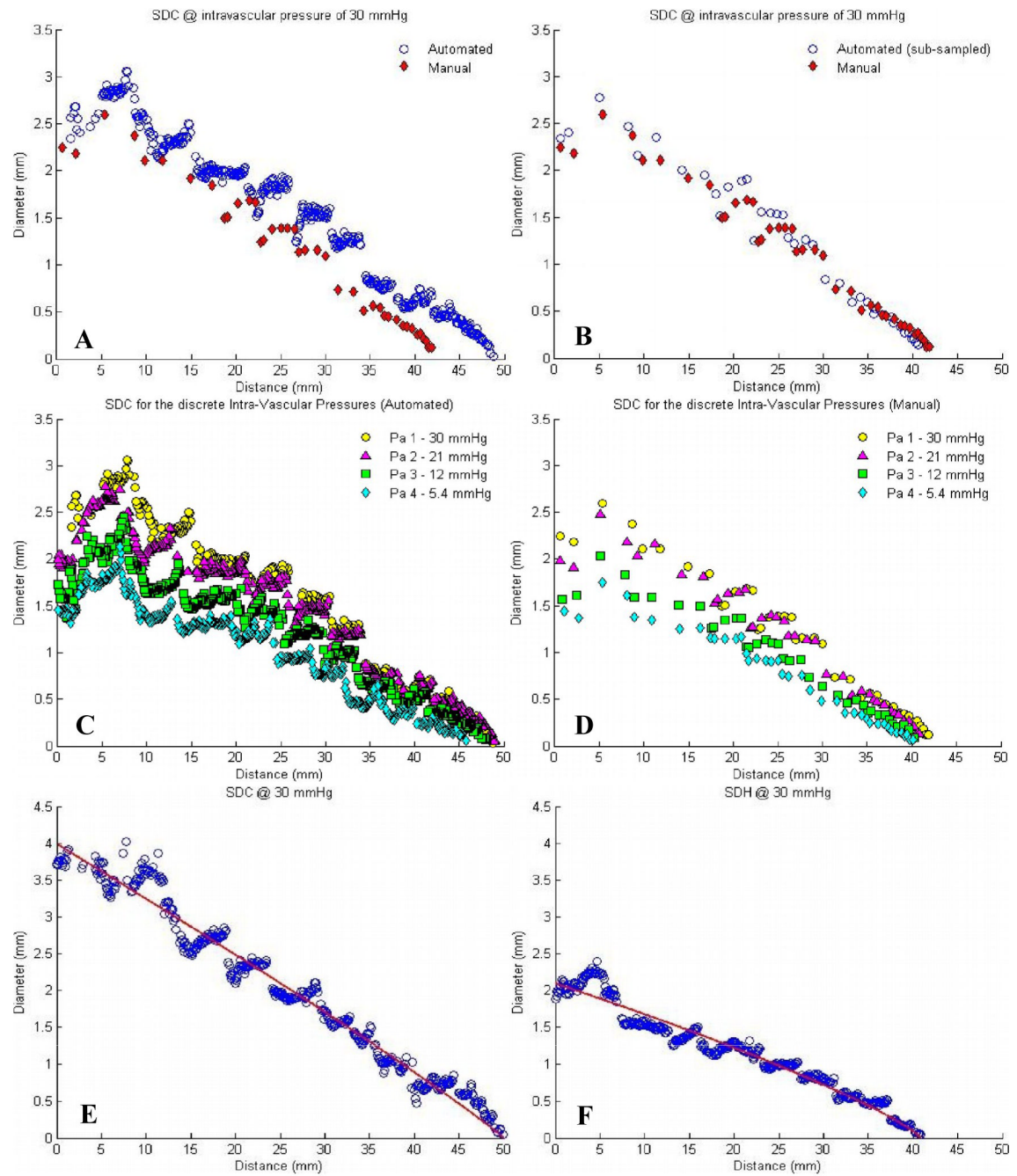


Figure 14.

Data displaying the diameter-distance relationship along the main trunk of example lungs.

A: Comparison of points measured by OGMT (◆ - Manual) vs. measured by the AVDMA (○ - Automated). **B:** Comparison of the OGMT (◆) data vs. sub-sampled AVDMA (○) data. **C, D:** Data for 4 intravascular pressures using (C) AVDMA and (D) OGMT methods. **E, F:** AVDMA (○) data for example (E) Sprague-Dawley Control (SDC) and (F) Sprague-Dawley Hypoxic (SDH) rat lungs fit to morphological model (Eq. 5) using a multi-parameter fitting technique (line).

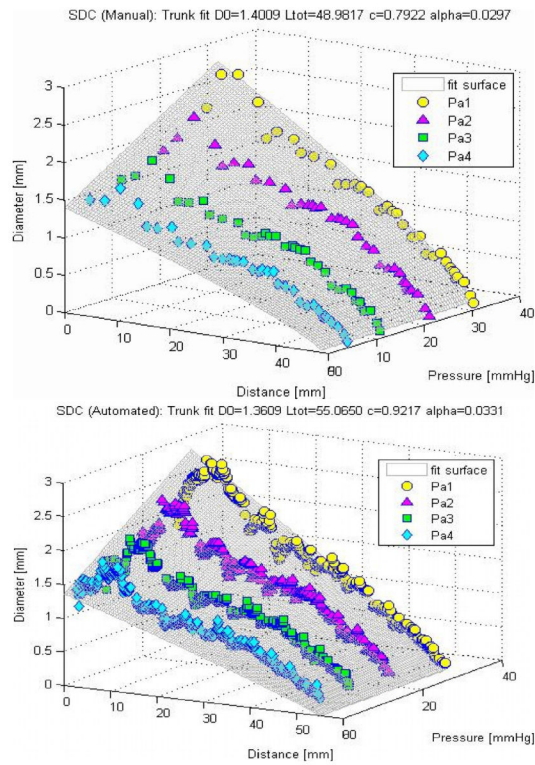


Figure 15.

Graphical representation of the rat pulmonary trunk morphology and biomechanics presented as diameter-distance curves at four arterial pressures for the OGMT (Manual, top) and AVDMA (Automated, bottom) techniques in a SDC rat. The surfaces represent the model fit (Eq. 7) to the main trunk data and the slant of the surface, along the pressure axis, is a reflection of the arterial distensibility.

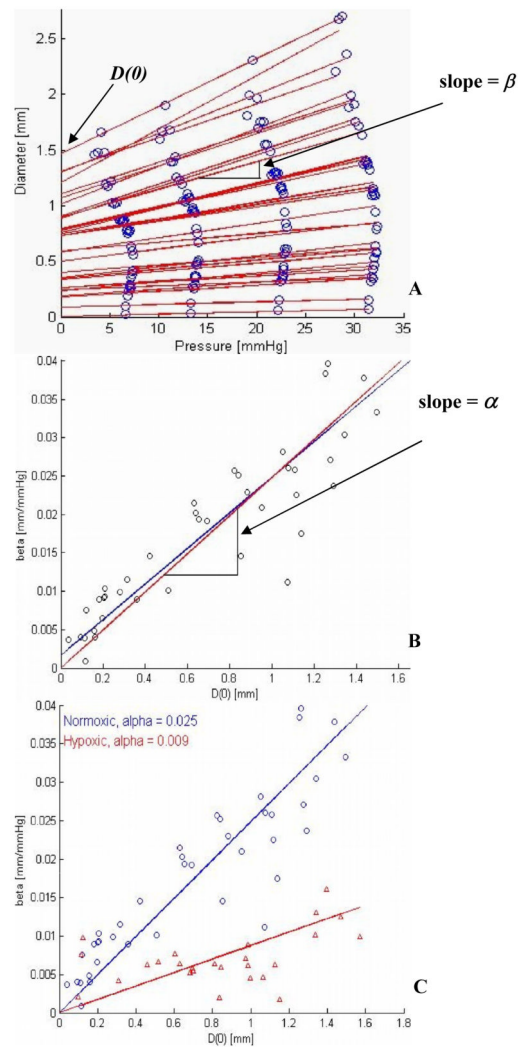


Figure 16.

Individual vessel method of calculating arterial distensibility. **A:** Pulmonary artery diameter vs. pressure plot for individual vessel segments from sub-sampled AVDMA SDC rat data. The slope of each regression line (vessel segments) is an estimate of the individual vessel distensibility (β) and $D(0)$ is an estimate of unstressed (Pressure = 0 mmHg) vessel diameter. **B:** β vs. $D(0)$ for all vessel segments from the sub-sampled AVDMA rat arterial data. The dark line represents the linear regression of the data. The lighter line represents the linear regression of the data using a zero intercept. Using an F-test, the slopes of all animals studied have been shown not to differ significantly. α is calculated as the slope of the lighter line. **C:** β vs. $D(0)$ from the sub-sampled AVDMA data for an example SDC ('o') vs. SDH ('Δ') rat.

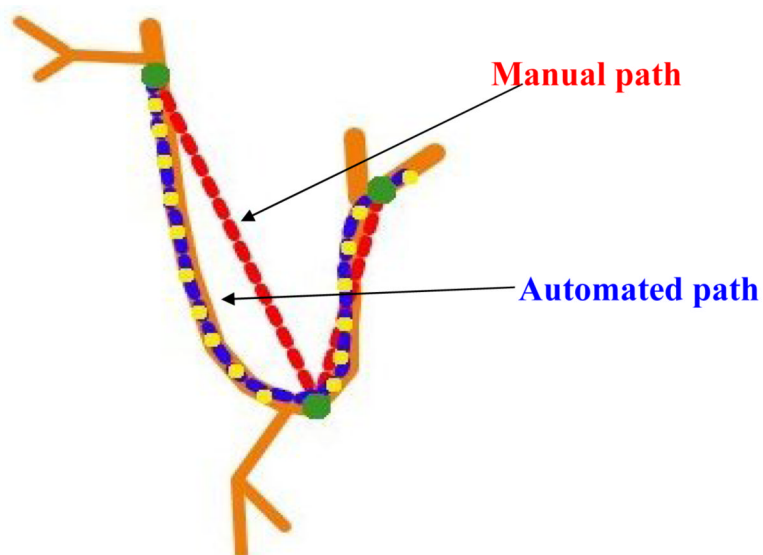


Figure 17.

Schematic of the distal portion (hook) of the main pulmonary arterial trunk illustrating the difference in trunk length calculation for different sampling densities. The path defined by OGMT (large dark dots) ends up being much shorter than the path defined by AVDMA (the smaller, lighter dots).

Table 1

Normalized root mean squared error (in percent) of subs-sampled AVDMA vs. OGMT data for Sprague-Dawley control (SDC) and CH (SDH) rats. Error data reported at each intravascular pressure and the average for each lung

Control	Pa1	Pa2	Pa3	Pa4	Average
SDC rat 1	4.896	4.032	5.459	3.687	4.518
SDC rat 2	4.769	4.015	3.149	3.829	3.940
SDC rat 3	3.534	4.458	4.665	2.720	3.844
SDC rat 4	4.881	3.908	6.727	8.615	6.033
Chronic Hypoxia					
SDH rat 1	4.988	6.289	4.589	4.663	5.132
SDH rat 2	3.228	4.029	7.608	6.827	5.423
SDH rat 3	4.993	4.898	3.079	2.245	3.804
SDH rat 4	4.439	3.986	3.783	4.149	4.089

Table 2

Comparison of morphometric parameters from SDC and SDH rats using various tree analysis techniques

OGMT	NORMOXIC (<i>N</i> = 4)	HYPOXIC (<i>N</i> = 4)
D ₀ (mm)	1.54 ± 0.05	1.51 ± 0.09
L _{tot} (mm)	44.2 ± 1.96	39.7 ± 0.76 *
C	0.94 ± 0.06	0.95 ± 0.07
α (mmHg ⁻¹)	0.0286 ± 0.001	0.0135 ± 0.001 *
Normalized error	0.0120 ± 0.002	0.0080 ± 0.001

AVDMA AUTOMATED	NORMOXIC (<i>N</i> = 4)	HYPOXIC (<i>N</i> = 4)
D ₀ (mm)	1.51 ± 0.13	1.61 ± 0.21
L _{tot} (mm)	53.7 ± 1.14	41.8 ± 2.23 *
C	0.97 ± 0.03	0.70 ± 0.06
α (mmHg ⁻¹)	0.0401 ± 0.002	0.0123 ± 0.001 *
Normalized error	0.0270 ± 0.006	0.0230 ± 0.006

AVDMA SUB-SAMPLED	NORMOXIC (<i>N</i> = 4)	HYPOXIC (<i>N</i> = 4)
D ₀ (mm)	1.62 ± 0.21	1.57 ± 0.19
L _{tot} (mm)	40.4 ± 0.75	35.2 ± 0.99 *
C	0.82 ± 0.07	0.69 ± 0.06
α (mmHg ⁻¹)	0.0296 ± 0.002	0.0113 ± 0.001 *
Normalized error	0.0190 ± 0.002	0.0180 ± 0.005

Values are Mean ± SE

* Significantly different from normoxic value (*p* < 0.05).

Table 3Comparison of estimations of arterial distensibility (α) in SDC and SDH rats

Experimental Group	α - AVDMA Multi-Parameter Fit (mmHg ⁻¹)	α -AVDMA Individual Vessel Fit (mmHg ⁻¹)	α -OGMT Individual Vessel Fit (mmHg ⁻¹)
SDC	0.0296 \pm 0.002	0.0252 \pm 0.003	0.0237 \pm 0.002
SDH	0.0113 \pm 0.001 *	0.0125 \pm 0.001 *	0.0130 \pm 0.001 *

Values are Mean \pm SE.

* Indicates significant different between SDC and SDH rats ($p < 0.05$). There is no significant difference between estimated from OGMT and AVDMA sub-sampled data ($p > 0.05$).